

# Revealing Short- and Long-range Li-ion diffusion in $\text{Li}_2\text{MnO}_3$ from finite-temperature dynamical mean field theory

Alex Taekyung Lee,<sup>1,2</sup> Kristin A. Persson,<sup>3,4</sup> and Anh T. Ngo<sup>1,2</sup>

<sup>1</sup>*Department of Chemical engineering, University of Illinois at Chicago, Chicago, IL 60608, USA*

<sup>2</sup>*Materials Science Division, Argonne National laboratory, Lemont, IL 60439, USA*

<sup>3</sup>*Environmental Energy Technologies Division, Lawrence Berkeley National Laboratory, Berkeley, California 94720, United States*

<sup>4</sup>*Department of Materials Science and Engineering, University of California Berkeley, Berkeley, California 94704, United States*

(Dated: February 4, 2026)

$\text{Li}_2\text{MnO}_3$  remains a crucial component of the Li-excess layered cathode family,  $(1-x)\text{LiMO}_2 + x\text{Li}_2\text{MnO}_3$  ( $M = \text{Mn, Ni, Co, \dots}$ ), but its role in limiting Li-ion mobility remains under debate. Here we combine DFT+ $U$ , finite-temperature DMFT with a continuous-time quantum Monte Carlo impurity solver, and nudged-elastic-band (NEB) calculations to investigate  $\text{Li}^+$  migration for a single Li vacancy in paramagnetic  $\text{Li}_2\text{MnO}_3$ . Dynamical electronic correlations within DMFT substantially reduce the activation energies of the lowest-barrier pathways, yielding  $E_a = 0.18$  eV for the shortest-range Li jump and  $E_a = 0.50$  eV for the next-lowest pathway. The 0.18 eV barrier quantitatively reproduces the short-range activation energy extracted from  $\mu^+\text{SR}$  measurements, whereas the 0.50 eV barrier is consistent with the long-range transport activation energy obtained from ac-impedance measurements. This single-vacancy, paramagnetic DMFT description therefore provides a coherent explanation of both local and macroscopic probes without requiring highly clustered vacancy configurations or strong extrinsic disorder, an assumption compatible with nearly stoichiometric  $\text{Li}_2\text{MnO}_3$  powders. Our results highlight the importance of finite-temperature dynamical correlations for Li-ion migration in correlated oxides and provide a framework for incorporating strong Coulomb interactions in future studies of transition-metal oxide battery materials.

## I. INTRODUCTION

Rising energy- and power-density targets for lithium-ion batteries have intensified the need for cathode materials that combine high capacity with strong rate capability [1–4]. Within the family of layered–layered Li-ion cathodes,  $\text{Li}_2\text{MnO}_3$  is a crucial component owing to its high operating voltage ( $\sim 4.4$ – $5.0$  V) and low cost [5–8]. Understanding the mechanisms and limitations of Li-ion mobility in  $\text{Li}_2\text{MnO}_3$  is therefore crucial for interpreting the performance of Li-rich layered oxides and for guiding the design of improved cathode architectures.

Experimental estimates of the Li-ion migration barrier in  $\text{Li}_2\text{MnO}_3$  span different probes and length scales [9–11]. At the microscopic (local) scale,  $\mu^+\text{SR}$  measurements on nearly stoichiometric  $\text{Li}_2\text{MnO}_3$  powders over 2–500 K determine a Li self-diffusion coefficient in the high-temperature paramagnetic regime ( $T \gg T_N$ ) and report a low activation energy,  $E_a = 0.156$  eV, for short-range Li jumps [10]. At the macroscopic scale, ac-impedance measurements on  $\text{Li}_2\text{MnO}_3$  ceramic powders [9] yield a substantially higher apparent barrier, with conductivity analyses giving  $E_a \approx 0.46$  eV for long-range Li-ion transport. Taken together, these experiments suggest a hierarchy of activation energies for local versus long-range Li motion in nominally pristine  $\text{Li}_2\text{MnO}_3$ .

First-principles nudged-elastic-band (NEB) studies based on density functional theory (DFT)+ $U$  have provided valuable insight into the topology of Li-ion migration pathways in  $\text{Li}_2\text{MnO}_3$  [12–15]. The DFT+ $U$ +NEB study by Shin *et al.* showed that, for  $\text{Li}^+$  migrating in the

presence of a single Li vacancy, the calculated barriers are 0.5–0.8 eV for intralayer hops and 0.64–0.65 eV for interlayer hops [12]. They further found that if  $\text{Li}^+$  migrates adjacent to a Li divacancy, the intralayer barrier drops to about 0.38 eV and the interlayer barrier to about 0.18 eV, while in the presence of a Li trivacancy the intralayer barrier can fall to  $\sim 0.05$  eV and the interlayer hop becomes effectively barrierless [12]. When compared with the microscopic (0.156 eV) and macroscopic (0.46 eV) experimental activation energies discussed above [9, 10], the barriers for  $\text{Li}^+$  migration in the presence of a single vacancy warrants further examination. Moreover, Li divacancies and trivacancies are unlikely to be abundant in the low-delithiation limit of nearly stoichiometric powder samples, such as those employed in the  $\mu^+\text{SR}$  and ac-impedance measurements of Sugiyama *et al.* and Nakamura *et al.* [9, 10].

A second limitation of much of the existing first-principles literature on  $\text{Li}_2\text{MnO}_3$  is its treatment of magnetism. In previous DFT+ $U$  studies, calculations have been performed within spin-polarized DFT+ $U$  assuming ferromagnetic order [14, 16, 17], in magnetically ordered states with the underlying spin configuration left unspecified [12, 15], or in a fully nonmagnetic (spin-unpolarized) state [6, 18]. However,  $\text{Li}_2\text{MnO}_3$  has a relatively low Néel temperature,  $T_N \approx 36$  K [19, 20], and is paramagnetic under the conditions relevant for Li-ion diffusion experiments and battery operation. Nonmagnetic calculations suppress local Mn moments entirely, whereas a true paramagnet exhibits zero net magnetization only as a result of thermal fluctuations of finite local mo-

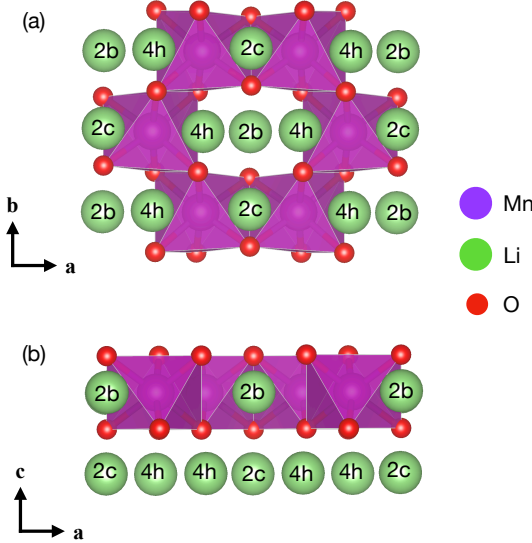


FIG. 1. Atomic structure of  $\text{Li}_2\text{MnO}_3$  with positions of Li ions.

ments. A finite-temperature framework that preserves local-moment physics- such as DFT combined with dynamical mean-field theory (DFT+DMFT) [21–24] - is therefore required to describe diffusion barriers in the experimentally relevant paramagnetic phase.

Owing to the low crystallographic symmetry of  $\text{Li}_2\text{MnO}_3$  (space group  $C2/m$ , No. 12), standard Wannier projections in the DFT+DMFT framework often produce effective Hamiltonians with substantial off-diagonal matrix elements, which can hinder DMFT from correctly reproducing the insulating gap of  $\text{Li}_2\text{MnO}_3$ . In our recent DFT+DMFT study of  $\text{Li}_2\text{MnO}_3$  [21], we identified an efficient strategy to accurately capture its electronic structure by diagonalizing the Mn- $d$  block. This approach demonstrates the viability of a low-energy,  $d$ -only model for  $\text{Li}_2\text{MnO}_3$ , in which the resulting Wannier basis implicitly encodes Mn- $d$ –O- $p$  hybridization.

In this work, we address these issues by combining DFT+ $U$ , DMFT with a quantum Monte Carlo impurity solver, and NEB calculations for a single Li vacancy in paramagnetic  $\text{Li}_2\text{MnO}_3$ . We first construct migration pathways using DFT+ $U$  NEB for six representative intra- and interlayer hops, and then evaluate DMFT total energies along these geometries, allowing the correlated electronic configuration to relax at each image. Dynamical electronic correlations substantially reduce the activation energies for the lowest-barrier paths, yielding  $E_a = 0.18$  eV for the lowest- $E_a$  interlayer hop and  $E_a = 0.50$  eV for the next-lowest intralayer path, while the barriers for the remaining paths within DMFT remain close to their DFT+ $U$  values. These two lowest barriers quantitatively reproduce the short-range activation energy from  $\mu^+$ SR and the long-range activation energy from ac-impedance measurements, establishing a unified

microscopic picture without invoking clustered vacancy configurations or strong extrinsic disorder.

### A. Computational methods

#### B. DFT+DMFT

We employ the non-charge-self-consistent DFT+DMFT method [25, 26] for relaxed structures obtained from DFT calculations. For DFT calculation, we use the projector augmented wave (PAW) method [27] and the revised version of the generalized gradient approximation (GGA) proposed by Perdew *et al.* (PBEsol) [28] as implemented in the VASP software [29]. Spin-independent version of the exchange correlation functional are employed. A plane wave basis with a kinetic energy cutoff of 500 eV is used. We used 48 atom unit cells (i.e.,  $1 \times 2 \times 2$  unit cells), which contains 8 Mn atoms, and  $\Gamma$ -centered  $\mathbf{k}$ -point meshes of size  $10 \times 5 \times 5$ . Atomic positions within the unit cells were relaxed until the residual forces were less than 0.01 eV/Å, and the stress was relaxed below 0.02 kB.

We solve the many-body problem on the manifold of Mn 3d-only orbitals, which is more efficient to reproduce the experimental energy gap ( $E_g$ ) [21]. The DFT+DMFT calculation has the following steps. First, we solve the non-spin-polarized Kohn-Sham (KS) equation within DFT using VASP. Second, we construct a localized-basis Hamiltonian for the Mn 3d bands by generating maximally localized Wannier functions (MLWFs) [30] for the nonmagnetic DFT band structure. The energy window employed ranges from  $E_F = -2.0$  eV to  $E_F + 4.0$  eV for the  $d$ -only basis. Finally, we solve the DMFT self-consistent equations for the correlated subspace of Mn 3d Wannier orbitals using the continuous time quantum Monte Carlo (CTQMC) [31, 32] impurity solver.

The rotationally invariant Coulomb interaction in the form of the Slater-Kanamori interaction Hamiltonian [33–35] is

$$\hat{H}_{\text{SK}} = U \sum_{\alpha} \hat{n}_{\alpha\uparrow} \hat{n}_{\alpha\downarrow} + \frac{1}{2} \sum_{\alpha \neq \beta} \sum_{\sigma \sigma'} (U' - J \delta_{\sigma\sigma'}) \hat{n}_{\alpha\sigma} \hat{n}_{\beta\sigma'} - \sum_{\alpha \neq \beta} (J c_{\alpha\uparrow}^{\dagger} c_{\alpha\downarrow} c_{\beta\downarrow}^{\dagger} c_{\beta\uparrow} + J' c_{\beta\uparrow}^{\dagger} c_{\beta\downarrow} c_{\alpha\uparrow}^{\dagger} c_{\alpha\downarrow}). \quad (1)$$

Here,  $c_{\sigma}$  and  $c_{\sigma}^{\dagger}$  denote the fermion annihilation and creation operators, where  $\sigma$  is the spin.  $U$  denotes an intra-orbital density-density interaction parameter,  $U'$  is an inter-orbital density-density interaction parameter,  $J$  is a spin-flip interaction parameter, and  $J'$  is a pair-hopping interaction parameter.  $U' = U - 2J$  and  $J' = J$  are due to rotational invariance.

Within DFT+DMFT framework [26], the self-energy convergence is achieved when  $\Sigma^{\text{loc}}(i\omega) = \Sigma^{\text{imp}}(i\omega)$ , where

$\Sigma^{\text{loc}}(i\omega)$  and  $\Sigma^{\text{imp}}(i\omega)$  are local and lattice self-energies, respectively, and  $i\omega$  is imaginary frequency.  $\Sigma$  is approximated as a local quantity in the correlated subspace. DFT+DMFT total energy is given by

$$E^{\text{TOT}} = E^{\text{DFT}}(\rho) + \sum_{m,\mathbf{k}} \epsilon_m(\mathbf{k}) \cdot [n_{mm}(\mathbf{k}) - f_m(\mathbf{k})] + E^{\text{POT}} - E^{\text{DC}}, \quad (2)$$

where  $E^{\text{DFT}}$  is the total energy from non spin-polarized DFT, and  $\epsilon_m(\mathbf{k})$  are the DFT eigenvalues.  $n_{mm}(\mathbf{k})$  and  $f_m(\mathbf{k})$  are the diagonal DMFT occupancy matrix element and Fermi function, respectively, for  $m$ th KS band and momentum  $\mathbf{k}$ . The potential energy  $E^{\text{POT}}$  is calculated by using Migdal-Galiski formula [36]:

$$E^{\text{POT}} = \frac{1}{2} \sum_{\omega} [\Sigma^{\text{loc}}(i\omega) \cdot G^{\text{loc}}(i\omega)]. \quad (3)$$

Here, the local Green's function is simplified by  $G^{\text{loc}}(i\omega) = \sum_{\mathbf{k}} G^{\text{loc}}(\mathbf{k}, i\omega)$ .

To obtain the spectral function, the maximum entropy method is used for the analytic continuation. Spectral function  $A(\omega)$  is given by

$$A(\omega) = -\frac{1}{\pi} \text{Im} \left[ \sum_{\mathbf{k}} G^{\text{loc}}(\mathbf{k}, \omega) \right]. \quad (4)$$

Large off-diagonal terms in the Hamiltonian can lead to significant errors within the DMFT method, as continuous time quantum Monte Carlo (CTQMC) only treats the diagonal terms to circumvent the sign problem. The non-parallel alignment of the cartesian axes of the Wannier orbitals and the directions of the Mn-O bonds arises from the  $C_{2h}$  point group symmetry of the MnO<sub>6</sub> octahedron [Fig. 1]. In cases where the point group symmetry of the transition metal (TM) octahedron is non-cubic, such as trigonal or monoclinic, there is a substantial mixing of the  $d$  basis ( $d_{xy}$ ,  $d_{xz}$ ,  $d_{yz}$ ,  $d_{z^2}$ ,  $d_{x^2-y^2}$ ), as these bases are defined within the cubic crystal field framework. Consequently, the off-diagonal terms of the Wannier Hamiltonian with the cubic  $d$  orbital basis become significant, leading to errors within the DMFT calculations. To resolve this issue, we diagonalize Mn  $d$  blocks of the Hamiltonian by applying a unitary rotation matrix, which is successful to reproduce the experimental energy gap [21].

Within DMFT, number of  $d$  electrons in Mn ( $N_d$ ), is computed from the local Green function  $G^{\text{loc}}(\mathbf{k}, \mathbf{k}', i\omega)$ :

$$N_d = \sum_{a,\omega} \sum_{\mathbf{k},\mathbf{k}'} \text{Im} \{ [\phi_d^a(\mathbf{k})]^* G^{\text{loc}}(\mathbf{k}, \mathbf{k}', i\omega) \phi_d^a(\mathbf{k}') \}, \quad (5)$$

where  $\phi_d^a(\mathbf{k})$  is the normalized  $d$ -orbital wavefunction, which is transformed from the wavefunction in the real space  $\phi_d^a(\mathbf{r})$  with the center of coordinates  $\mathbf{r}$  on a transition metal ion.

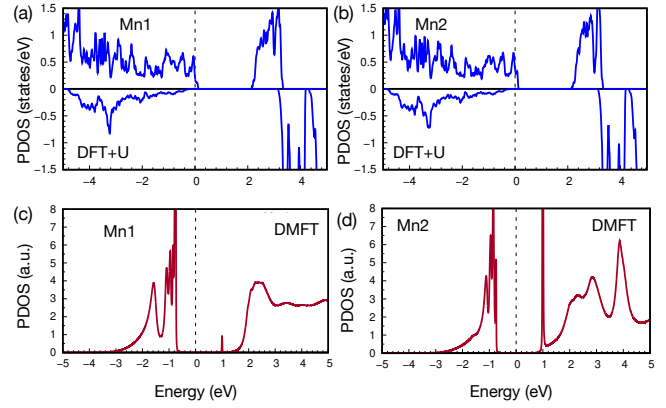


FIG. 2. Electronic structure of Li<sub>2</sub>MnO<sub>3</sub> with a single Li vacancy from DFT+ $U$  and DMFT. (a,b) DFT+ $U$  projected density of states (PDOS) onto Mn1 and Mn2  $d$  states. (c,d) DMFT PDOS projected onto the Mn- $d$ -like correlated subspace on Mn1 and Mn2. Mn1 and Mn2 denote inequivalent Mn sites. We caution that in the downfolded DMFT setup the correlated orbitals are Mn- $d$ -like Wannier functions that implicitly include Mn-O hybridization; therefore changes in the projected Mn- $d$  occupancy reflect the effective low-energy description and should not be interpreted as a direct oxidation-state assignment in the full  $p$ - $d$  manifold.

### C. DFT+ $U$ and atomic structures

The GGA+ $U$  scheme within the rotationally invariant formalism together with the fully localized limit double-counting formula [37] is used to study the effect of electron interactions. We used  $U=4$  and  $J=0$  unless specified. Projected density of states (PDOS) are obtained by the spherical harmonic projections inside spheres around each atom. Wigner-Seitz radii of 1.323 Å were used for the projection of Mn atoms, respectively, as implemented in the VASP-PAW pseudopotential.

Both spin-unpolarized and spin-polarized versions of the exchange-correlation functional were employed in the DFT+ $U$  calculations. For each magnetic configuration, the structure was fully relaxed, including both internal atomic coordinates and lattice stresses. We used a  $1 \times 1 \times 2$  supercell to compare the relative energies of different magnetic phases within DFT+ $U$ , and a  $1 \times 2 \times 2$  supercell to compute Li migration paths in both the DFT+ $U$  and DMFT calculations.

## II. RESULTS AND DISCUSSION

### A. Electronic structure of Li<sub>2</sub>MnO<sub>3</sub> with single Li vacancy

First, we study the electronic properties of Li<sub>2</sub>MnO<sub>3</sub> with a single Li vacancy using DFT+ $U$ . There are three distinct Li sites,  $2b$ ,  $4h$ , and  $2c$ , as shown in Fig. 1. Using

a  $1 \times 1 \times 2$  supercell containing four Mn atoms, we compare the total energies of four collinear magnetic configurations: ferromagnetic (FM), A-type antiferromagnetic (A-AF), C-type antiferromagnetic (C-AF), and G-type antiferromagnetic (G-AF), for different Li-vacancy positions, where A-, C-, and G-type denote antiferromagnetic alignment along one, two, and three crystallographic directions defined by the conventional  $a$ ,  $b$ , and  $c$  lattice vectors. For each Li-vacancy configuration, the FM phase is more stable than the AF phases by 14–182 meV (see Table I in Appendix). Thus, in the Li-diffusion calculations employing a larger  $1 \times 2 \times 2$  supercell, we adopt the FM configuration.

Figure 2 shows the projected density of states (PDOS) onto Mn  $d$  states in  $\text{Li}_2\text{MnO}_3$  with a single Li vacancy. Removing one Li atom reduces the electron count by one (creating a single hole). We examine two inequivalent Mn sites: Mn1, adjacent to the vacancy ( $\text{Mn1-Li}_{\text{vac}} = 2.89 \text{ \AA}$ ), and Mn2, farther away ( $\text{Mn2-Li}_{\text{vac}} = 3.90 \text{ \AA}$ ). Within DFT+ $U$ , the Mn-projected spectra at Mn1 and Mn2 are nearly indistinguishable [Fig. 2(a,b)]: no sharp in-gap state forms, and the weight near the valence-band maximum (VBM) remains broadly distributed. Consistently, the integrated Mn- $d$  occupations vary only weakly,  $N_d(\text{Mn1}) = 4.88$  and  $N_d(\text{Mn2}) = 4.89$ , indicating that the vacancy does not produce a strongly site-selective change within the Mn- $d$  manifold at this level of theory. In line with prior DFT+ $U$  and hybrid-functional studies [6, 16, 38], the vacancy-induced change at the VBM is primarily associated with O 2p states (ligand-hole character), rather than the formation of a well-defined  $\text{Mn}^{5+}$  oxidation state.

In contrast, the  $d$ -only DMFT results [Fig. 2(c,d)] show a strongly site-dependent redistribution of spectral weight within the Mn- $d$ -like correlated subspace. Relative to Mn1, Mn2 exhibits a pronounced depletion of occupied Mn- $d$  weight together with an increase of unoccupied weight near  $E_F$ , while the Mn1-projected spectrum remains comparatively unchanged. The corresponding Mn- $d$ -like occupations are  $N_d(\text{Mn1}) = 3.00$  and  $N_d(\text{Mn2}) = 2.01$  (nominal values within the reduced correlated subspace), i.e., the dominant reduction of the Mn- $d$ -like occupation occurs on Mn2. We emphasize that in this downfolded description the O degrees of freedom are not treated explicitly; their influence is incorporated through renormalized crystal fields and hoppings of the Mn- $d$ -like Wannier basis. Therefore, the apparent Mn-centered site dependence should be interpreted as a property of the effective low-energy representation, not as direct evidence for a literal integer-valence Mn oxidation-state change in the full  $p$ - $d$  electronic structure. A definitive real-space assignment of oxygen- versus manganese-centered hole character would require a fully charge-self-consistent  $p$ - $d$  correlated subspace, which is considerably more computationally demanding and is left for future work. This difference between DFT+ $U$  and DMFT in the correlated-subspace charge rearrangement in the presence of the vacancy also suggests that the two meth-

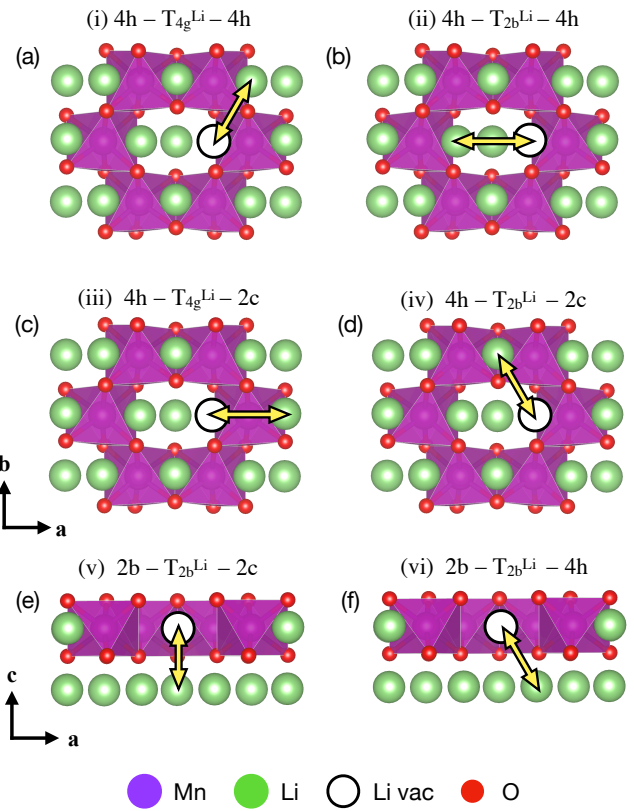


FIG. 3. Diffusion path of single Li vacancy in  $\text{Li}_2\text{MnO}_3$ . (a)-(d) intra layer diffusion. (e)-(f) inter layer diffusion.

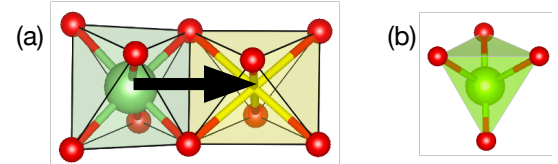


FIG. 4. (a) Diffusion path (ii) of single Li vacancy in  $\text{Li}_2\text{MnO}_3$ , and (b)  $\text{LiO}_4$  tetrahedral structure at the saddle point.

ods can yield different Li-ion migration barriers. Since DMFT modifies the electronic response along the migration coordinate via dynamical correlations (as quantified below through the total-energy decomposition), the resulting migration barrier can differ from that obtained in static DFT+ $U$ .

## B. Li-ion migration barriers: DFT+ $U$ versus DMFT

Next, we analyze  $\text{Li}^+$  migration in  $\text{Li}_2\text{MnO}_3$  using DFT+ $U$  and DMFT. We consider six symmetry-inequivalent pathways defined in Fig. 3: four *intralayer*

hops (i)  $4h - T_{4g}^{\text{Li}} - 4h$ , (ii)  $4h - T_{2b}^{\text{Li}} - 4h$ , (iii)  $4h - T_{4g}^{\text{Li}} - 2c$ , (iv)  $4h - T_{2b}^{\text{Li}} - 2c$ , and two *interlayer* hops (v)  $2b - T_{2b}^{\text{Li}} - 2c$ , (vi)  $2b - T_{2b}^{\text{Li}} - 4h$ . These paths are similar to those considered in a previous DFT+*U* study [12]. The corresponding activation energies  $E_a$  are summarized in Fig. 5 (blue: DFT+*U*; red: DMFT). We first obtain the migration paths and saddle points using NEB within DFT+*U* (blue curves), and then evaluate the energies of the initial, final, and saddle-point configurations using DMFT (red symbols). Because the *d*-only DMFT setup can yield multiple low-energy, site-dependent electronic solutions within the Mn-*d*-like correlated subspace for a given ionic geometry, we initialize distinct DMFT solutions on several Mn sites and select the lowest-energy converged solution for each NEB image.

Within DFT+*U*, the migration barriers for intralayer diffusion are  $E_a = 0.63$ – $0.93$  eV. In all cases,  $\text{Li}^+$  migrates via the tetrahedral interstitial site ( $T$ ), forming a  $\text{LiO}_4$  tetrahedron at the saddle point, as shown in Fig. 4, consistent with previous work [12]. The barriers along paths (i) and (iii) are relatively large,  $E_a = 0.90$  and  $0.93$  eV, respectively, in reasonable agreement with the earlier DFT+*U* values of  $0.78$  and  $0.80$  eV [12]; the remaining differences are likely due to details of the computational setup (e.g., supercell size and choice of parameters). In contrast, the barriers along paths (ii) and (iv) are lower,  $E_a = 0.68$  and  $0.63$  eV, indicating that path (iv) provides the lowest intralayer migration barrier. The earlier DFT+*U* study also found  $E_a = 0.60$  and  $0.56$  eV for paths (ii) and (iv), respectively, likewise identifying path (iv) as the lowest-barrier pathway. For interlayer diffusion within DFT+*U*, the barriers are  $E_a = 0.65$  and  $0.67$  eV for paths (v) and (vi), respectively, which are slightly larger than the lowest intralayer diffusion barrier.

Next, we compute  $E_a$  using DMFT at  $300$  K in the paramagnetic phase. As in DFT+*U*, the lowest- $E_a$  diffusion paths are (ii)  $4h - T_{2b}^{\text{Li}} - 4h$  and (iv)  $4h - T_{2b}^{\text{Li}} - 2c$ , but DMFT notably reduces the corresponding barriers, as shown in Fig. 5. The DMFT activation energies for paths (ii) and (iv) are  $0.18$  and  $0.50$  eV, respectively, while for the remaining paths the DFT+*U* and DMFT barriers differ by only  $0.02$ – $0.15$  eV. We note that in the present DMFT setup, the correlated subspace is defined by Mn-*d*-like Wannier functions that implicitly include Mn–O hybridization; consequently, the vacancy-induced charge rearrangement is represented within this effective low-energy manifold.

The lowest barrier of  $0.18$  eV corresponds to a short-range Li jump between neighboring sites within the  $\text{Li}_2\text{MnO}_3$  region. This value is close to the experimental activation energy  $E_a = 0.156$  eV obtained from  $\mu^+\text{SR}$  measurements, which probe local Li self-diffusion in nearly stoichiometric  $\text{Li}_2\text{MnO}_3$  powders [10]. Our DMFT results therefore suggest that the experimentally observed short-range activation scale can be rationalized by single-vacancy migration along the lowest-barrier pathway in the paramagnetic phase, without invoking Li divacancies or trivacancies.

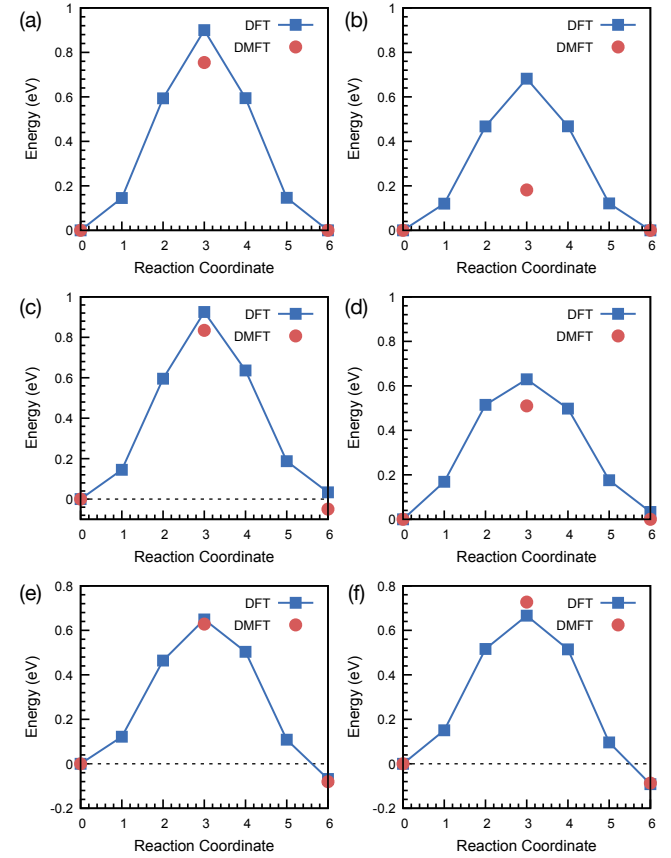


FIG. 5. (a)–(f) Migration barriers for a single Li vacancy in  $\text{Li}_2\text{MnO}_3$  along pathways (i)–(vi), respectively.

From ac-impedance measurements on  $\text{Li}_2\text{MnO}_3$  powder samples, which probe long-range Li-ion transport, Nakamura *et al.* reported an activation energy of  $E_a = 0.46$  eV at  $900$  °C [9]. In our DMFT barrier landscape, the  $0.18$  eV hop by itself does not form a percolating pathway for net Li transport out of the  $\text{Li}_2\text{MnO}_3$  region [Fig. 5(b)]; long-range migration requires additional hops. Among these, the intralayer path (iv) has the lowest barrier,  $E_a = 0.50$  eV, while the other paths are higher. Thus, an energetically favorable long-range route consists of many low-barrier ( $0.18$  eV) hops combined with occasional  $0.50$  eV hops, for example  $4h - T_{2b}^{\text{Li}} - 4h - T_{2b}^{\text{Li}} - 2c$ , and the overall rate is controlled by the larger barrier,  $E_a \approx 0.50$  eV. Despite the different experimental temperature, the controlling barrier is of the same order as the activation energy extracted from ac-impedance measurements, indicating a comparable bottleneck scale for long-range transport.

To study the origin of the  $E_a$  reduction within DMFT, we analyze the change in the total energy  $E^{\text{TOT}}$  (Eq. 2) between the initial and saddle-point configurations for the lowest-barrier path (ii). For the underlying DFT contribution  $E^{\text{DFT}}$ , the saddle point lies  $0.678$  eV higher in energy than the initial

state. In contrast, the DMFT eigenvalue correction term,  $\sum_{m,\mathbf{k}} \epsilon_m(\mathbf{k}) [n_{mm}(\mathbf{k}) - f_m(\mathbf{k})]$ , stabilizes the saddle point: this term is lower in energy at the saddle than at the initial configuration by 0.507 eV, thereby substantially reducing the net barrier. Interestingly, the energy differences between initial and saddle point in non-spin-polarized DFT and in spin-polarized DFT+ $U$  are 0.678 and 0.681 eV, respectively, indicating that the static Hubbard  $U$  in DFT+ $U$  has only a minor effect on  $E_a$ . Although the eigenvalue correction provides the dominant DMFT contribution, the remaining terms  $E^{\text{POT}}$  and  $E^{\text{DC}}$  in Eq. 2 are small: the saddle point is higher in energy by only 0.07 eV in  $E^{\text{POT}}$ , and  $E^{\text{DC}}$  changes by only  $-0.45$  meV, with the saddle point slightly lower in energy. Thus, the lowering of the migration barrier within DMFT is dominated by the eigenvalue correction term, rather than by changes in the static interaction or double-counting energies.

Physically, the dominant *eigenvalue-correction* contribution quantifies how the DMFT  $\mathbf{k}$ -resolved density matrix  $n_{mm}(\mathbf{k})$  deviates from the DFT reference Fermi occupations  $f_m(\mathbf{k})$ , weighted by the underlying DFT eigenvalues  $\epsilon_m(\mathbf{k})$ . The fact that this term is markedly lower at the tetrahedral saddle point indicates that dynamical correlations encoded in the DMFT self-energy drive a more favorable charge redistribution within the Mn- $d$ -like correlated subspace along the migration coordinate, consistent with more effective electronic polarization/screening of the migrating Li $^+$  in the saddle-point configuration and thus a reduced activation barrier.

Having established that the dominant DMFT contribution to the barrier reduction is electronic, we next examine whether the underlying ionic pathway exhibits a large local distortion or a qualitative change of the Mn-projected spectra between the initial and saddle-point structures. Here we emphasize that the DMFT energies are evaluated on the fixed DFT+ $U$  NEB geometries (i.e., the same ionic pathway used in the energetic decomposition), so any change in  $E_a$  arises from the electronic functional rather than from a different relaxed migration pathway.

Along path (ii), the Mn–O distances around the Mn site showing the largest change of Mn- $d$ -like occupation in DMFT (denoted Mn4) vary only weakly between the initial and saddle configurations: the six Mn–O bonds change by at most  $\sim 0.025$  Å at the saddle point, while the remaining bonds change by  $\lesssim 0.013$  Å. Consistent with this modest structural variation, the Mn4-projected spectra retain the same overall features between the initial and saddle-point structures in both DFT+ $U$  and DMFT, with only minor redistributions of spectral weight near the band edges (Fig. 6). Together, these observations support that the reduced migration barrier in DMFT primarily originates from the correlated electronic contribution to the total energy evaluated on an essentially unchanged ionic pathway, rather than from a qualitatively different lattice relaxation.

### III. SUMMARY

In this work, we investigated Li-ion migration in Li<sub>2</sub>MnO<sub>3</sub> by combining DFT+ $U$ , DFT+DMFT (with a continuous-time quantum Monte Carlo solver), and nudged-elastic-band (NEB) calculations for a single Li vacancy in the paramagnetic phase. By evaluating DMFT total energies on the fixed DFT+ $U$  NEB geometries for six representative intra- and interlayer paths—and optimizing the correlated electronic state at each NEB image—we find that dynamical correlations reduce the activation energies for the lowest-barrier paths to  $E_a = 0.18$  eV for path (ii) and  $E_a = 0.50$  eV for path (iv), while leaving the other paths largely unchanged relative to DFT+ $U$ . The lowest barrier,  $E_a = 0.18$  eV, is close to the microscopic activation energy for short-range Li self-diffusion extracted from  $\mu^+$ SR measurements on nearly stoichiometric Li<sub>2</sub>MnO<sub>3</sub> powders, suggesting that the local activation scale can be rationalized by single-vacancy migration along path (ii) in a paramagnetic host, without invoking Li divacancies or trivacancies.

Long-range transport, on the other hand, necessarily involves sequences of hops that combine low-barrier (0.18 eV) and higher-barrier (0.50 eV) steps; within such a network, the effective activation energy is controlled by the larger barrier,  $E_a \approx 0.50$  eV. Despite the different experimental temperature, this controlling scale is of the same order as the macroscopic activation energies obtained from ac-impedance measurements on ceramic powders. Our results also indicate that interpretations based solely on interlayer diffusion are too restrictive, and that a mixture of intra- and interlayer processes is required to reconcile local and macroscopic probes.

These findings highlight the importance of beyond-DFT treatments for ionic diffusion in correlated oxides, and motivate future extensions to higher vacancy concentrations and mixed-cation Li-rich layered cathodes. In particular, extending the present framework to regimes where oxygen redox becomes active will be essential for assessing how lattice defects, charge redistribution, and dynamical correlations jointly influence transport and stability.

### IV. ACKNOWLEDGMENT

This research is supported by the Vehicle Technologies Office (VTO), Department of Energy (DOE), USA, through the Battery Materials Research (BMR) program. We also acknowledge financial support from the U.S. Department of Energy, Office of Science, Office of Basic Energy Sciences, Materials Science and Engineering Division. We gratefully acknowledge the computing resources provided on Improv, a high-performance computing cluster operated by the Laboratory Computing Resource Center at the Argonne National Laboratory.

---

[1] J. B. Goodenough and Y. Kim, *Chemistry of Materials* **22**, 587 (2010).

[2] J. B. Goodenough and K.-S. Park, *Journal of the American Chemical Society* **135**, 1167 (2013), pMID: 23294028, <https://doi.org/10.1021/ja3091438>.

[3] A. Manthiram, *ACS Central Science* **3**, 1063 (2017).

[4] A. Manthiram, *Nature Communications* **11**, 1550 (2020).

[5] N. Yabuuchi, K. Yoshii, S.-T. Myung, I. Nakai, and S. Komaba, *Journal of the American Chemical Society* **133**, 4404 (2011), pMID: 21375288, <https://doi.org/10.1021/ja108588y>.

[6] D.-H. Seo, J. Lee, A. Urban, R. Malik, S. Kang, and G. Ceder, *Nature Chemistry* **8**, 692 (2016).

[7] D. Ye and L. Wang, *Materials Technology: Advanced Performance Materials* **29**, A59 (2014).

[8] G. Liu and S. Zhang, *International Journal of Electrochemical Science* **11**, 5545 (2016).

[9] K. Nakamura, H. Hirano, Y. Michihiro, and T. Moriga, *Solid State Ionics* **181**, 1359 (2010).

[10] J. Sugiyama, K. Mukai, H. Nozaki, M. Harada, M. Månsson, K. Kamazawa, D. Andreica, A. Amato, and A. D. Hillier, *Phys. Rev. B* **87**, 024409 (2013).

[11] H. Yu, Y. Wang, D. Asakura, E. Hosono, T. Zhang, and H. Zhou, *RSC Advances* **2**, 8797 (2012).

[12] Y. Shin, H. Ding, and K. A. Persson, *Chem. Mater.* **28**, 2081 (2016).

[13] F. Kong, R. C. Longo, M.-S. Park, J. Yoon, D.-H. Yeon, J.-H. Park, W.-H. Wang, S. KC, S.-G. Doo, and K. Cho, **3**, 8489, publisher: The Royal Society of Chemistry.

[14] S. Wang, J. Liu, and Q. Sun, *J. Mater. Chem. A* **5**, 16936 (2017).

[15] T. Sarkar, K. R. Prakasha, M. D. Bharadwaj, and A. S. Prakash, *Phys. Chem. Chem. Phys.* **19**, 31724 (2017).

[16] R. Xiao, H. Li, and L. Chen, *Chemistry of Materials* **24**, 4242 (2012).

[17] H. Chen and M. S. Islam, *Chemistry of Materials* **28**, 6656 (2016).

[18] K. Hikima, K. Shimizu, H. Kiuchi, Y. Hinuma, K. Suzuki, M. Hirayama, E. Matsubara, and R. Kanno, *Journal of the American Chemical Society* **144**, 236 (2022), pMID: 34957828, <https://doi.org/10.1021/jacs.1c09087>.

[19] P. Strobel and B. Lambert-Andron, *Journal of Solid State Chemistry* **75**, 90 (1988).

[20] S. Lee, S. Choi, J. Kim, H. Sim, C. Won, S. Lee, S. A. Kim, N. Hur, and J.-G. Park, *Journal of Physics: Condensed Matter* **24**, 456004 (2012).

[21] A. T. Lee, H. Park, and A. T. Ngo, *Phys. Rev. B* **108**, 205146 (2023).

[22] J. Molenda, P. Wilk, and J. Marzec, *Solid State Ionics* **146**, 73 (2002).

[23] D. M. Korotin, D. Novoselov, and V. I. Anisimov, *Phys. Rev. B* **99**, 045106 (2019).

[24] E. B. Isaacs and C. A. Marianetti, *Phys. Rev. B* **102**, 045146 (2020).

[25] H. Park, R. Nanguneri, and A. T. Ngo, *Phys. Rev. B* **101**, 195125 (2020).

[26] V. Singh, U. Herath, B. Wah, X. Liao, A. H. Romero, and H. Park, *Computer Physics Communications* **261**, 107778 (2021).

[27] P. E. Blöchl, *Phys. Rev. B* **50**, 17953 (1994).

[28] J. P. Perdew, A. Ruzsinszky, G. I. Csonka, O. A. Vydrov, G. E. Scuseria, L. A. Constantin, X. Zhou, and K. Burke, *Phys. Rev. Lett.* **100**, 136406 (2008).

[29] G. Kresse and D. Joubert, *Phys. Rev. B* **59**, 1758 (1999).

[30] N. Marzari, A. A. Mostofi, J. R. Yates, I. Souza, and D. Vanderbilt, *Rev. Mod. Phys.* **84**, 1419 (2012).

[31] K. Haule, *Phys. Rev. B* **75**, 155113 (2007).

[32] E. Gull, A. J. Millis, A. I. Lichtenstein, A. N. Rubtsov, M. Troyer, and P. Werner, *Rev. Mod. Phys.* **83**, 349 (2011).

[33] J. C. Slater, *Phys. Rev.* **82**, 538 (1951).

[34] J. Kanamori, *Prog. Theor. Phys.* **30**, 275 (1963).

[35] A. Georges, L. d. Medici, and J. Mravlje, *Annu. Rev. Condens. Matter Phys.* **4**, 137 (2013).

[36] V. Galitskii and A. Migdal, *me Teoret. Fiz.* **34** (1958).

[37] A. I. Liechtenstein, V. I. Anisimov, and J. Zaanen, *Phys. Rev. B* **52**, R5467 (1995).

[38] K. Hoang, *Phys. Rev. Appl.* **3**, 024013 (2015).

## V. APPENDIX A

TABLE I. Relative energies (in eV) of collinear magnetic configurations within DFT+ $U$  for different Li-vacancy positions in the  $1 \times 1 \times 2$  supercell. Here  $E$  denotes the total energy of a given configuration,  $\Delta E = E - E_{\min}$  is measured with respect to the global ground state (FM with a Li vacancy at the  $2b$  site), and  $\delta E = E - E_{\text{FM}}(\text{Li-vac})$  is measured with respect to the FM state for the same Li-vacancy position.

Li-vac site	Magnetic order	$\Delta E$ (eV)	$\delta E$ (eV)
$2b$	FM	0.000	0.000
	A-AF	0.014	0.014
	C-AF	0.140	0.140
	G-AF	0.145	0.145
$4h$	FM	0.065	0.000
	A-AF	0.079	0.065
	C-AF	0.179	0.165
	G-AF	0.196	0.182
$2c$	FM	0.043	0.000
	A-AF	0.086	0.043
	C-AF	0.218	0.175
	G-AF	0.216	0.173

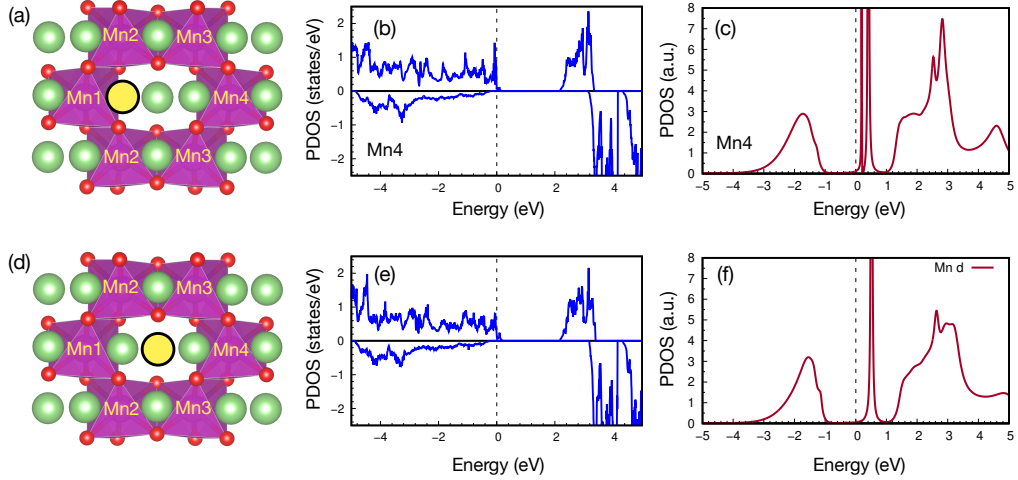


FIG. 6. PDOS onto Mn4 in  $\text{Li}_2\text{MnO}_3$  within DFT+ $U$  and DMFT, (a)-(c) at the initial configuration and (d)-(f) at the saddle point